Nano Energy 62 (2019) 239–249

Contents lists available at ScienceDirect

Nano Energy

journal homepage: www.elsevier.com/locate/nanoen

Full paper

Hierarchical nanosheets constructed by integration of bimetallic sulfides into N-Doped carbon: Enhanced diffusion kinetics and cycling stability for sodium storage

Xiaodan Li[a], Wendi Zhang[a,b], Jiangxiang Cai[a], Hejin Yan[b], Mengqi Cui[b], Gaoxiang Wu[c], Meicheng Li[b,*]

[a] Fujian Provincial Key Laboratory of Functional Materials and Applications, School of Materials Science and Engineering, Xiamen University of Technology, Xiamen, 361024, China
[b] State Key Laboratory of Alternate Electrical Power System with Renewable Energy Sources, North China Electric Power University, Beijing, 102206, China
[c] State Grid Chongqing Electric Power Co.Electric Research Science Institute, Chongqing, 401123, China

ARTICLE INFO

Keywords:
Bimetallic sulfides
MOFs
DFT calculation
Sodium-ion batteries

ABSTRACT

Transition metal sulfides (TMS) are considered as anode candidates for sodium-ion batteries (SIBs) due to the high theoretical specific capacity and natural abundance. Herein, Co_3S_4@1T MoS_2/NC-L hierarchical nanosheets, in which bimetallic sulfides are integrated into N-doped carbon, has been designed and prepared via calcination of leaf-like Co-ZIF (ZIF-L) precursor followed by hydrothermal sulfuration reaction. When evaluated as anode for SIBs, the Co_3S_4@1T MoS_2/NC-L hierarchical nanosheets offer enhanced pseudocapacitance effect, fast Na^+ kinetics in the heterogenous interface of bimetallic sulfides and small polarization, achieving an delightful reversible capacity of 595 mAh g^{-1} at 0.1 A g^{-1} and rate capability of 338 mA h g^{-1} at 5 A g^{-1}. Moreover, the fine structural stability and mutual affinity of bimetallic sulfides under high cutoff voltage hinder the loss of sodium polysulfide during conversion reaction, promoting the long cycling stability of hierarchical nanosheets. Such bimetallic sulfides/N-doped carbon hierarchical nanosheet sheds new light on the construction of efficient anode material for SIBs.

1. Introduction

Sodium-ion batteries have stimulated increasing research interest as promising energy-storage devices for large-scale energy storage systems, since the similar electrochemical property but abundant reserve and low cost of sodium versus those of lithium [1,2]. However, the larger ionic radius of sodium (~1.06 Å vs. ~0.76 Å of Li) leads to poor electrochemical reaction kinetics, limiting the energy density and rate capability of SIBs [3,4]. Thus, the design of suitable electrode materials, especially high-performance anode materials exerts significant effects on improving the electrochemical performance of SIBs.

Compared to intercalation materials [5,6] and metal oxides [7,8], transition metal sulfides (TMS) [9–11] have attracted prominent attention due to the higher theoretical specific capacity through the conversion reaction mechanism, superior intrinsic conductivity and more suitable redox potential. Especially, the metallic 1T MoS_2 possesses remarkable electronic conductivity, expanding interlayer spacing, and numerous active sites for ion insertion/extraction [12–14]. The interlayer expansion of 1T MoS_2 has been demonstrated to be associated with a lower diffusion energy barrier for Na^+, resulting in an improvement of the storage capacity and rate performance for SIBs [15]. However, the two-dimensional (2D) MoS_2 layers tend to stack and aggregate spontaneously, giving raise to the reduction of electrochemical active sites along the basal plane. Moreover, the large volume changes derived from aggregated MoS_2 layers and loss of polysulfide intermediates during repeated discharge/charge normally result in rapid capacity fading upon cycling and low Coulombic efficiencies.

To address above issues, one promising strategy is construction of proper hierarchical nanostructures, which can reduce the stack/aggregation of MoS_2 nanosheets and shorten the Na^+ diffusion pathways simultaneously [16–18]. Incorporating TMS with carbonaceous material is also considered to be an effective approach to accommodate the stress of volume expansion and inhibit the loss of polysulfide intermediates during the sodiation/desodiation processes, thus maintaining the cycling stability [19–21]. Zeolitic imidazolate frameworks (ZIFs) with 2D leaf-like structures and fine thermal stability are good

* Corresponding author.
E-mail address: mcli@ncepu.edu.cn (M. Li).

https://doi.org/10.1016/j.nanoen.2019.05.040
Received 22 April 2019; Received in revised form 13 May 2019; Accepted 14 May 2019
Available online 15 May 2019

candidates as precursor/template to construct carbon-based metal sulphides hierarchical nanostructures [22–24]. The integration of 2D leaf-like ZIF and 2D MoS_2 layers into hierarchical porous nanosheets brings out a large amount of active surfaces and shortened diffusion lengths for charge storage. Benefiting from the thermal stability, the organic bridging ligands of ZIFs can in-situ transform into heteroatoms-doped carbon matrix after calcination in inert environments, which helps to improve electronic transport and ion diffusion kinetics.

In this study, the integration of bimetallic sulfides into N-Doped Carbon was realized by calcination of leaf-like Co-ZIF (ZIF-L) precursor and hydrothermal sulfuration reaction, successfully constructing Co_3S_4@1T MoS_2/NC-L hierarchical nanosheets. Such hierarchical nanosheet offers shortened ion diffusion path and much exposed active sites for sodium storage. The carbon matrix and its abundant nitrogen-doped species are beneficial to the electronic conductivity and pseudo-capacitive behavior. Moreover, density functional theory (DFT) calculation reveals that the heterogenous interface of bimetallic sulfides offers favorable adsorption sites for sodium storage and facilitates Na^+ diffusion kinetics compared to pure 1T MoS_2 layers. Correspondingly, the Co_3S_4@1T MoS_2/NC-L hierarchical nanosheets obtained both long cyclic stability and high specific capacity at high cutoff voltage.

2. Results and discussion

The formation of the Co_3S_4@1T MoS_2/NC-L hierarchical nanosheet was proposed in Scheme 1. At first, the Co-ZIF-L precursor with tens of nanometers thickness and micro-scale planar size (Fig. 1a and Fig. S1) was synthesized in aqueous solutions at room temperature. Then, the as-obtained Co-ZIF-L was calcinated at 650 °C in nitrogen atmosphere, forming a composite of Co nanocrystals embedded N-doped carbon which well inherits the 2D leaf-like structure (Co/NC-L template, Fig. 1b and Fig. S1). During subsequent hydrothermal process, the sulfidation of Co and growth of expanding 1T MoS_2 were occurred in or on Co/NC-L nanosheets. Meanwhile, partial N atoms of Co/NC-L template infiltrate into the carbon derived from glucose, resulting in a new-formed N-doped carbon layer on the surface of these 1T MoS_2 layers. Overall, the Co_3S_4 nanocrystals and 1T MoS_2 layers were confined in N-Doped Carbon matrix, constructing the Co_3S_4@1T MoS_2/NC-L hierarchical nanosheet.

According to the scanning electron microscopy (SEM) images, these Co_3S_4@1T MoS_2/NC-L hierarchical nanosheets (Fig. 1c) possess the similar planar size but incremental thickness compared to Co-ZIF-L precursor. The surface of these hierarchical nanosheets presents a meshed pattern assembled by typical MoS_2 layers. In addition, the hydrothermal product in absent of molybdenum source, Co_3S_4/NC-L (Fig. 1d), visually displays a nanosheet with cobalt sulfide nanoparticles derived from the sulfuration of Co in the Co/NC-L template. For comparison, pure MoS_2/C sample was also prepared without the addition of Co/NC-L template, as shown in Fig. 1e. It exhibits a sphere-like structure with a diameter of ≈400 nm, which is aggregation of multiple layers. In this respect, the Co_3S_4@1T MoS_2/NC-L hierarchical nanosheet with expanding MoS_2 layers expose more surface active sites, which can promote a rapid electron and ions mobility for the near-surface sodium storage [16]. The chemical compositions of these samples were investigated by X-ray diffraction (XRD). In Fig. 1f, XRD pattern of Co_3S_4/NC-L indicates a relatively poor crystallization of Co_3S_4 nanoparticles and the diffraction peaks at 26.7° , 31.4 °, 38.0° and 55.0° can be indexed to the (220), (311), (400) and (440) planes of linnaeite Co_3S_4 (PDF card 42–1448), respectively. As for Co_3S_4@1T MoS_2/NC-L, except for the characteristic peaks of Co_3S_4, most of the other diffraction peaks can be assigned to a 2H–MoS_2. However, it is observed that the (002) peak of the as-prepared MoS_2 at 9.2° is lower than that of 2H–MoS_2 at 14.4°, and an additional diffraction peak appears at 18.1° [25,26]. This result implies an enlarged interlayer spacing of MoS_2 and promising existence of metallic 1T phase of MoS_2.

The hierarchical structure of the Co_3S_4@1T MoS_2/NC-L was further

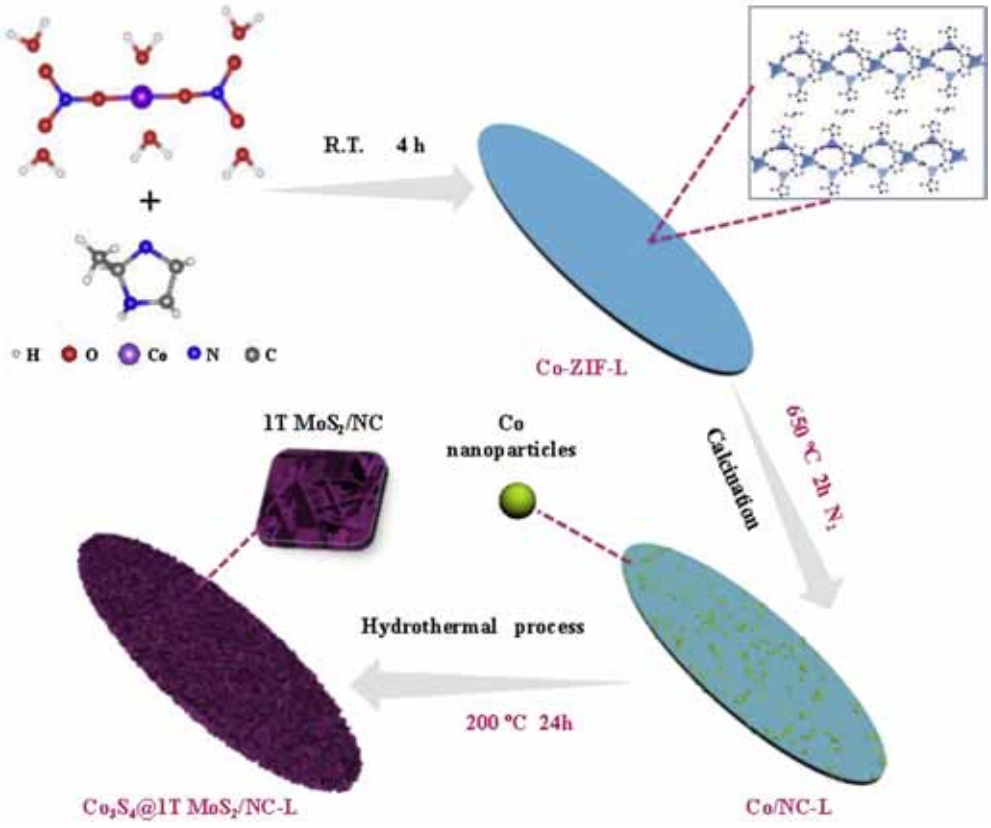

Scheme 1. Illustration of the fabrication process of the Co_3S_4@1T MoS_2/NC-L hierarchical nanosheets.

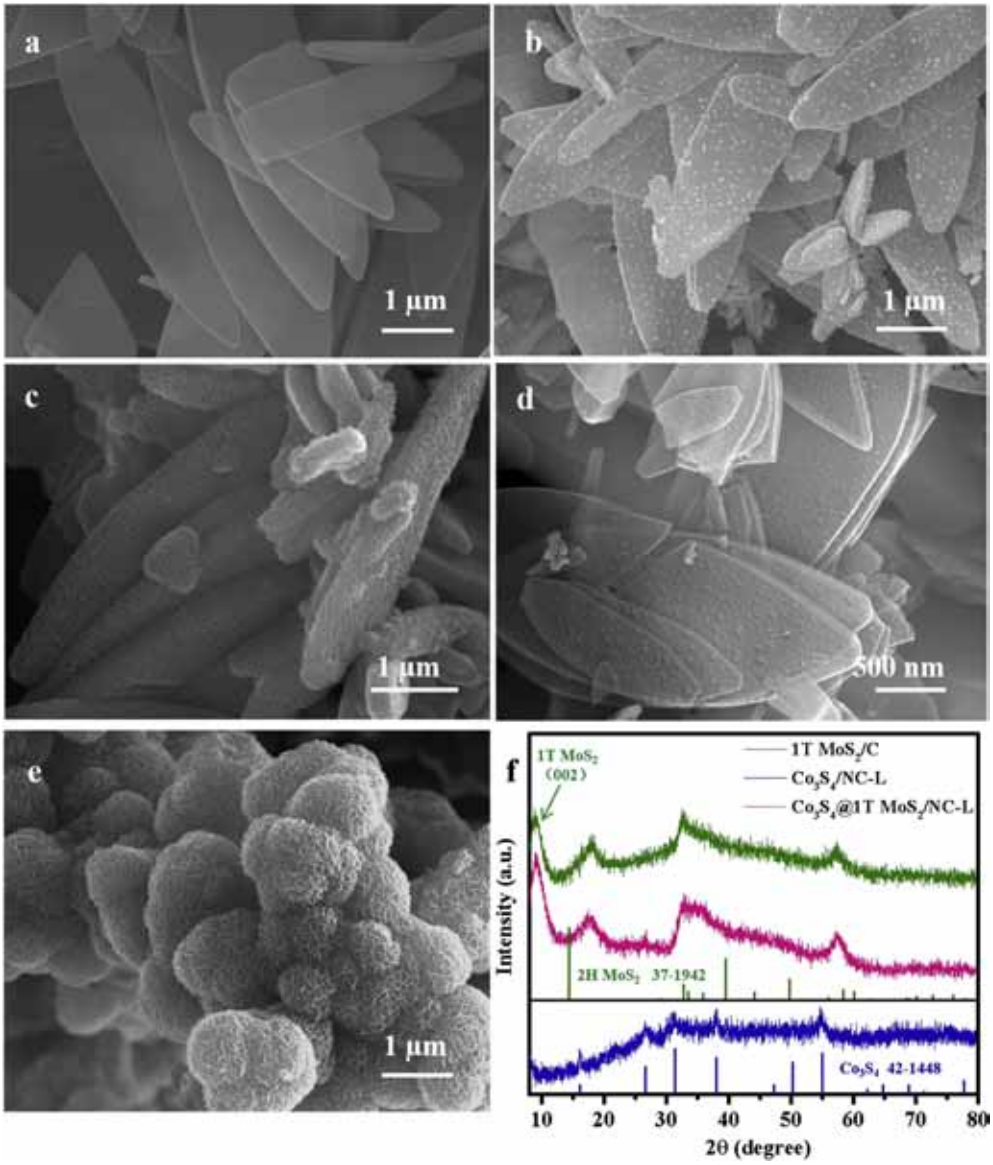

Fig. 1. Morphology and structure characterization. a) SEM image of Co-ZIF-L precursor. b) SEM image of Co/NC-L. c) SEM image of Co_3S_4@1T MoS_2/NC-L hierarchical nanosheets. d) SEM image of Co_3S_4/NC-L. e) SEM image of 1T MoS_2/C. f) XRD patterns of Co_3S_4@1T MoS_2/NC-L, Co_3S_4/NC-L, 1T MoS_2/C and standard patterns of JCPDS Cards.

confirmed by the TEM observation, as shown in Fig. 2. Specifically, the hierarchical nanosheets is a leaf-liked carbon matrix with internal dispersive Co_3S_4 nanoparticles and external expanding MoS_2 layers. It is notable that the outer edge of MoS_2 layers is covered by amorphous carbon. In the high resolution TEM (HRTEM) image, the average interlayer spacing of MoS_2 is 0.67 nm (~0.62 nm of 2H MoS_2), which is consistent with the low-angle shift of the diffraction peak related to (002) plane. The lattice fringes with a spacing of 0.28 nm are consistent with the (311) plane of the Co_3S_4 phase. The corresponding Fourier transform pattern further displays that the diffraction spots correspond to the (440), (311) planes of the linnaeite Co_3S_4. The EDS elemental mapping demonstrates the uniform distribution of S, N, C, Mo, Co in the hierarchical nanosheet. Especially, the corresponding location of C and N in the HADDF image indicates that N atoms even uniformly doped into the amorphous carbon outside the MoS_2 layers. It is assumed that partial N atoms of Co/NC-L template permeate outwards, and deposit together with carbon derived from glucose on the outside of the MoS_2 layers during hydrothermal sulfidation. Thus, the Co_3S_4 nanocrystals and MoS_2 nanosheets were confined in a sheet-shaped N-Doped Carbon matrix, constructing the hierarchical nanosheet.

The nitrogen adsorption-desorption test was performed to study the porosity of the as-prepared samples. As shown in Fig. 3a, the mesoporous structure of Co_3S_4@1T MoS_2/NC-L was confirmed by the type-IV adsorption-desorption isotherm with a H3 hysteresis loop [27,28]. According to the Brunauer-Emmett-Teller (BET) method, the specific surface area of Co_3S_4@1T MoS_2/NC-L, Co_3S_4/NC-L and MoS_2/C are 38.3 $cm^2 g^{-1}$, 7.0 $cm^2 g^{-1}$ and 12.3 $cm^2 g^{-1}$, respectively. Fig. 3b exhibits their pore size distributions derived from the Barrett-Joyner-Halenda (BJH) model. The Co_3S_4@1T MoS_2/NC-L presents most 2–10 nm pores than other two samples, mainly due to more interspaces between the expanding MoS_2 nanoblocks in the hierarchical nanosheet. These interspaces are importance to increase the electrochemical active sites and decrease the volume changes during repeated sodium insertion/extraction. In contrast, the compact stacking of pure MoS_2 nanoblocks or Co_3S_4/NC-L nanosheets results in the low specific surface area and porosity in the other two samples.

The compositions and surface chemical states of the as-prepared samples were investigated by Raman spectroscopy and X-ray

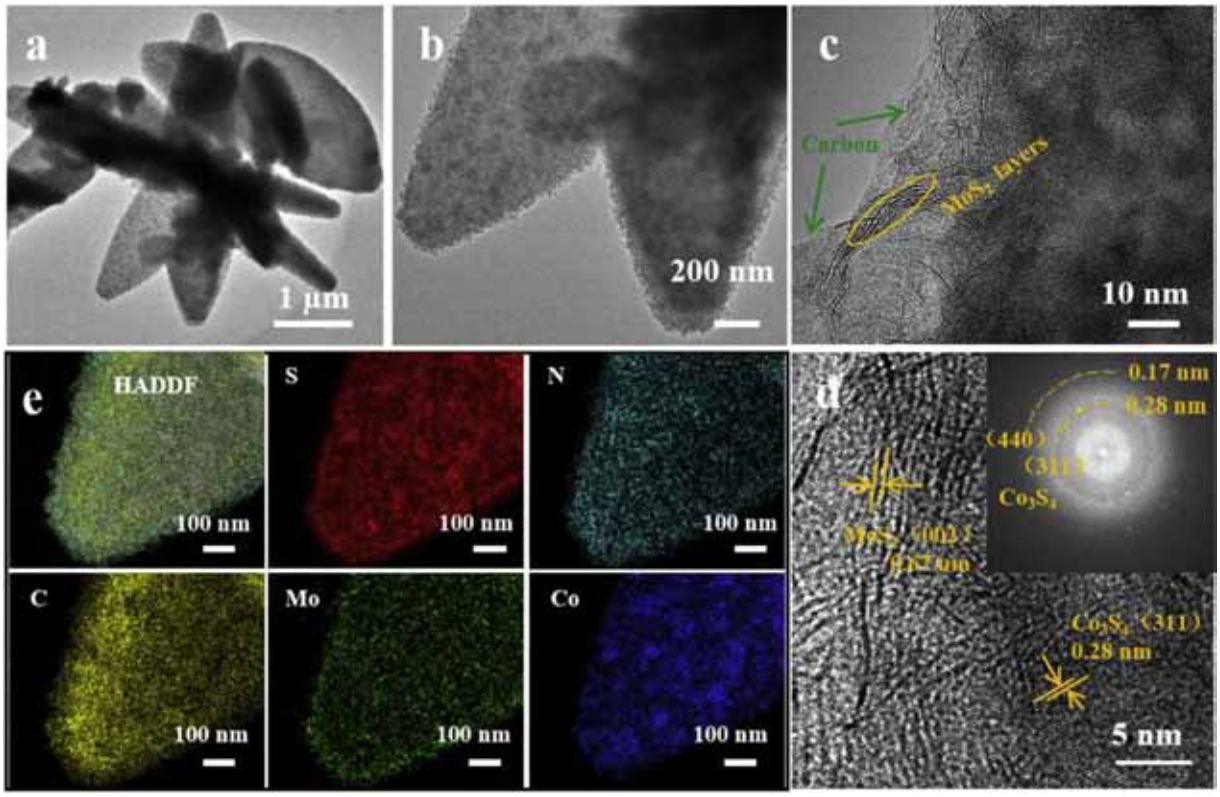

Fig. 2. Detailed hierarchical structural characterization. a, b) TEM images of Co_3S_4@1T MoS_2/NC-L. c, d) HRTEM images of Co_3S_4@1T MoS_2/NC-L and e) the HADDF image of C, N and EDX mapping images of S, N, C, Mo and Co.

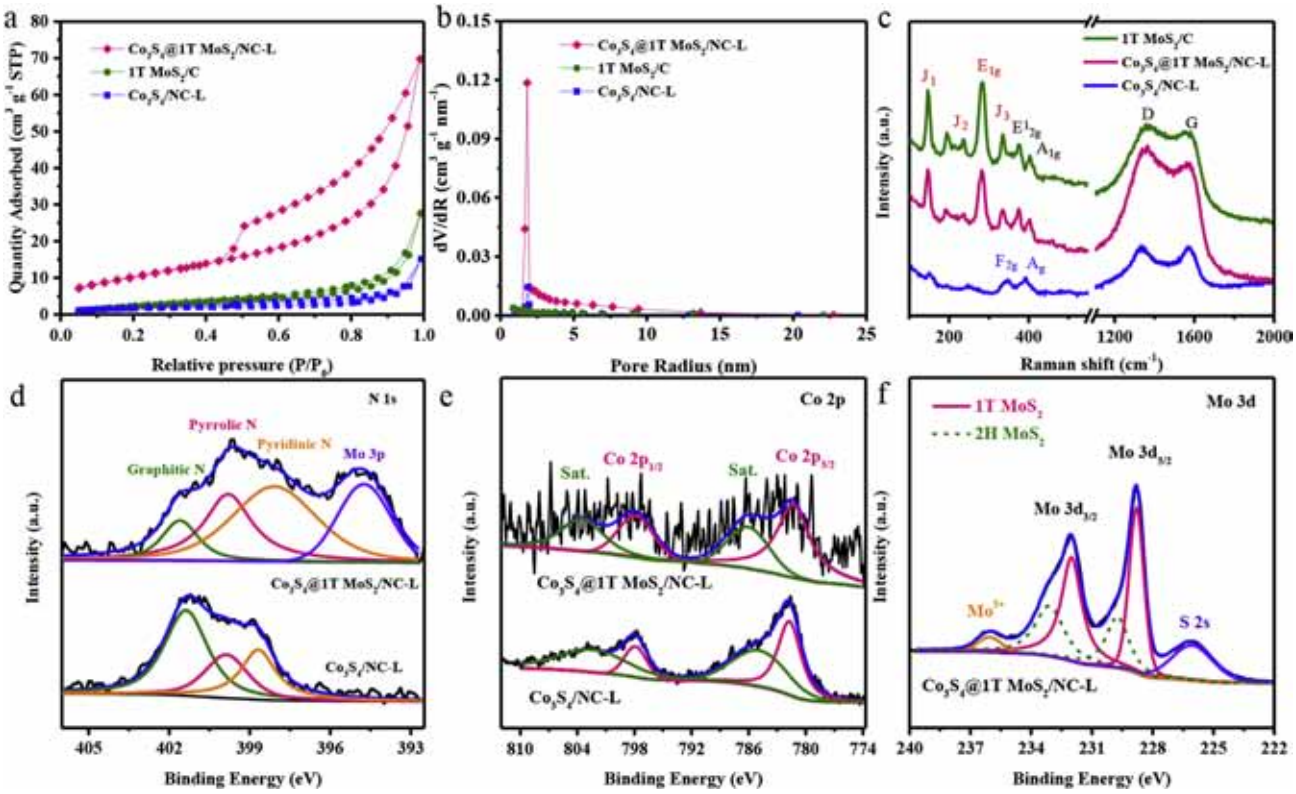

Fig. 3. The porosity and composition characteristic. a) Nitrogen adsorption-desorption isotherms of Co_3S_4@1T MoS_2/NC-L, 1T MoS_2/C and Co_3S_4/NC-L. b) Corresponding pore size distributions of the three samples. d) Raman spectra of the three samples. d-f) XPS spectra of Co_3S_4@1T MoS_2/NC-L and Co_3S_4/NC-L.

photoelectron spectroscopy (XPS). In Fig. 3c, these Raman signals show the characteristic E^1_{2g} (376.2 cm^{-1})/A_{1g} (402.4 cm^{-1}) peaks of MoS_2 and F_{2g} (348.1 cm^{-1})/A_g (392.2 cm^{-1}) modes of Co_3S_4, respectively [29,30]. In particular, the additional J_1, J_2, J_3 and E_{1g} peaks located at 148.0, 236.2, 334.5 and 283.6 cm^{-1} are observed in as-prepared MoS_2-containing samples. The E_{1g} signal denotes the octahedrally coordinated Mo in 1T MoS_2 and the presence of J_1, J_2, J_3 peaks is mostly attributed to superlattice distortion in the basal plane of 1T MoS_2, confirming the formation of 1T-phase MoS_2 [25,31]. Furthermore, the D peak and G peak of amorphous carbon are observed in the Raman spectra of Co_3S_4@1T MoS_2/NC-L, Co_3S_4/NC-L and even MoS_2/C. The value of I_D/I_G indicates the degree of disorder/defect in the carbon matrix, which could be calculated by Gaussian fitting and integrated areas of these peaks [24,32], as exhibited in Figs. S2a–c. The value is in the order of MoS_2/C (~2.53) > Co_3S_4@1T MoS_2/NC-L (~1.35) > Co_3S_4/NC-L (~0.84) (Table S1). It reveals that the external carbon formed by hydrothermal process possesses more defects for enhancing the Na-storage, while the internal carbon template via calcination at 650 °C exhibits more graphitized order for enhanced carrier mobility.

In the high-resolution C1s XPS spectra (Fig. S3), three peaks with binding energies of 284.7, 286.2 ± 0.2, and 288.7 ± 0.2 eV are associated with C–C, C–N/O, and C=O, respectively [33,34]. The existence of C–O is due to slight surface oxidization of the samples exposed to air before measurement. The formation of C–N bond stems from the nitrogenous bridging ligands of Co-ZIFs-L precursor. The states of nitrogen doping in Co_3S_4@1T MoS_2/NC-L and Co_3S_4/NC-L were further confirmed by the N 1s spectra in Fig. 3d. The Mo 3p signal at binding energies of 394.7 eV emerges in the N 1s spectrum of Co_3S_4@1T MoS_2/NC-L is due to the existence of MoS_2. Three types of nitrogen species corresponding to pyridinic N, pyrrolic N, and graphitic N are well identified in Co_3S_4@1T MoS_2/NC-L and Co_3S_4/NC-L, respectively [22]. The nitrogen contents in carbon matrix and the proportion of three species for the two samples are displayed in Table S2. Compared to Co_3S_4/NC-L, the lower nitrogen content of Co_3S_4@1T MoS_2/NC-L is attributed to the additional carbon formed by glucose during hydrothermal process. Furthermore, partial N atoms diffuse outwards to the additional carbon in the Co_3S_4@1T MoS_2/NC-L under hydrothermal conditions, which shows significant impact on the proportion of different nitrogen species. Thus, the higher proportion of pyridinic N and pyrrolic N was obtained in Co_3S_4@1T MoS_2/NC-L, contributing to more defect sites for the enhanced carrier transport [22]. The high-resolution Co 2p spectra in Fig. 3e can be deconvoluted into four characteristic peaks of Co $2p_{1/2}$, Co $2p_{3/2}$ and their satellite peaks [12,35]. The Co 2p peak of Co_3S_4@1T MoS_2/NC-L is much weaker than that of Co_3S_4/NC-L, attributing to a uniformly thick coverage of the MoS_2 layers. Since the present of 1T and 2H phases of as-prepared MoS_2 is confirmed by Raman spectra, the Mo 3d spectrum of Co_3S_4@1T MoS_2/NC-L in Fig. 3f should contain two doublets for Mo $3d_{5/2}$ and Mo $3d_{3/2}$. It is reported that the binding energies of 2H MoS_2 are slightly higher than that of 1T MoS_2 [36,37]. Accordingly, one doublet located at 228.8 eV and 232.0 eV are corresponding to Mo $3d_{5/2}$ and Mo $3d_{3/2}$ for the 1T phase, and the other doublet at 229.7 eV and 233.0 eV are for the 2H phase. The S 2p spectra in Fig. S3c present two peaks assigned to S $2p_{3/2}$ and S $2p_{1/2}$. It is observed that a pair of peaks by deconvolution slightly shifted to lower binding energies due to the formation of 1T MoS_2 in the Co_3S_4@1T MoS_2/NC-L. The content of the 1T MoS_2 in Co_3S_4@1T MoS_2/NC-L is evaluated to be 67.5%, according to the deconvoluted Mo 3d regions [37,38].

The unique 2D hierarchical geometry with highly active bimetallic sulfides and highly conductive N-doped carbon makes Co_3S_4@1T MoS_2/NC-L a promising electrode material for SIBs. To evaluate the electrochemical performance of Co_3S_4@1T MoS_2/NC-L, it was assembled into half-cells with Na metal as counter electrode. Fig. 4a presents the initial five CV curves of Co_3S_4@1T MoS_2/NC-L electrode. Four peaks are observed in the first cathodic scan, and the electrochemical process of these peaks can be better identified by comparison with the CV cures of Co_3S_4/NC-L and 1T MoS_2/C (Fig. S4). The weak cathodic peak at 1.4 V is associated with the intercalation of Na ions into the Co_3S_4 crystals [22]. The other three peaks at 1.1 V, 0.5 V and 0.1 V are related to the formation of a solid-state interphase (SEI) layer, the intercalation of Na ions into MoS_2 interlays, and the conversion reaction into Mo/Na_2S [20,39]. The subsequent CV curves exhibit shifted cathodic peaks compared to the initial state. Especially, the signals correspond to the conversion reaction into metallic Co and the intercalation of Na ions into MoS_2 interlays are reflected in the peaks at ~0.9 V and 0.75 V [20,22]. The anodic peaks between 1.5 V and 2.0 V are attributed to the reversible oxidation of Na_2S and metals. These anodic/cathodic peaks are well overlapped, implying a good reversibility for Na^+ storage. Accordingly, the reaction processes of the Co_3S_4@1T MoS_2/NC-L hierarchical nanosheets occur as follows:

$$Co_3S_4 + xNa^+ + xe^- \leftrightarrow Na_xCo_3S_4 \quad (1)$$

$$Na_xCo_3S_4 + (8-x)Na^+ + 8e^- \leftrightarrow 4Na_2S + 3Co \quad (2)$$

$$MoS_2 + xNa^+ + xe^- \leftrightarrow Na_xMoS_2 \quad (3)$$

$$Na_xMoS_2 + (4-x)Na^+ + (4-x)e^- \leftrightarrow 2Na_2S + Mo \quad (4)$$

It is noteworthy that the process (4) can be fully conducted at about 0.01 V, but be a restricted reaction at 0.1 V. Considering the effect of restricted reaction on the electrochemical performance, the galvanostatic charge-discharge (GDC) measurement was conducted in the voltage window of 0.1-3 V. As displayed in Fig. 4b, the electrochemical processes in the GDC profiles at a current density of 0.1 A g^{-1} are well consistent with above CV results. The initial discharge and charge capacities are 1062 and 595 mA h g^{-1}, respectively, giving a relatively high CE of 56%. The initial irreversible capacity loss is largely due to the formation of SEI and irreversible phase transformation. The subsequent GDC profiles exhibit slight deviations and stable CEs of > 98%, indicating a good capacity reversibility for sodium storage. After 100 cycles (Fig. 4c), the Co_3S_4@1T MoS_2/NC-L electrode still delivers a reversible capacity of 536 mA h g^{-1}, which is nearly 90% capacity retention. For comparison, the first discharge and charge capacities of Co_3S_4/NC-L (as shown in Fig. S4) are 804 and 392 mA h g^{-1}, respectively, resulting in an initial CE of 49%. The reversible capacity of Co_3S_4/NC-L continuously decays during cycles, resulting in capacity retention of 52% and persistent CE of ~97% after 100 cycles. Thus, compared with Co_3S_4/NC-L, the enhanced reversible capacity and CE of Co_3S_4@1T MoS_2/CN-L are mainly due to the cooperation of expanding 1T MoS_2 layers.

The rate capability and long cycling performance of Co_3S_4@1T MoS_2/NC-L, Co_3S_4/NC-L and MoS_2/C are compared in Fig. 4d and e. The Co_3S_4@1T MoS_2/NC-L hierarchical nanosheet delivers high specific capacities of 619, 557, 517, 480, 438 and 338 mA h g^{-1} at the current densities of 50, 200, 500, 1000, 2000 and 5000 mA g^{-1}, respectively (Fig. 4d). Thereafter, the specific capacity returns to 601 mA h g^{-1} when the current density shortly reduces back to 50 mA h g^{-1}, demonstrating a remarkable capacity recovery. Comparatively, the Co_3S_4/NC-L electrode shows poorer rate capability, which are mainly correlated with continuous capacity fading and theoretical capacity limitation. As for MoS_2/C electrode, the capacity is high but decays rapidly at low current densities. It is proposed that the restricted conversion reaction to Mo/Na_2S can be stimulated at low current densities or small polarization to achieve high capacity, but the sodium polysulfide derived from this reaction simultaneously resulting in capacity decay. When the conversion reaction is gradually restricted under high current density, the cycling stability is obviously improved. Under high current density of 500 mA g^{-1}, the Co_3S_4@1T MoS_2/NC-L shows improved capacity of 368 mAh g^{-1} and enhanced cycling stability after 300 cycles. The morphology of the Co_3S_4@1T MoS_2/NC-L after 300 cycles (Fig. S5) retain the 2D sheet-shaped structure in which bimetallic sulfides are uniformly dispersed. In comparison, the specific capacity of

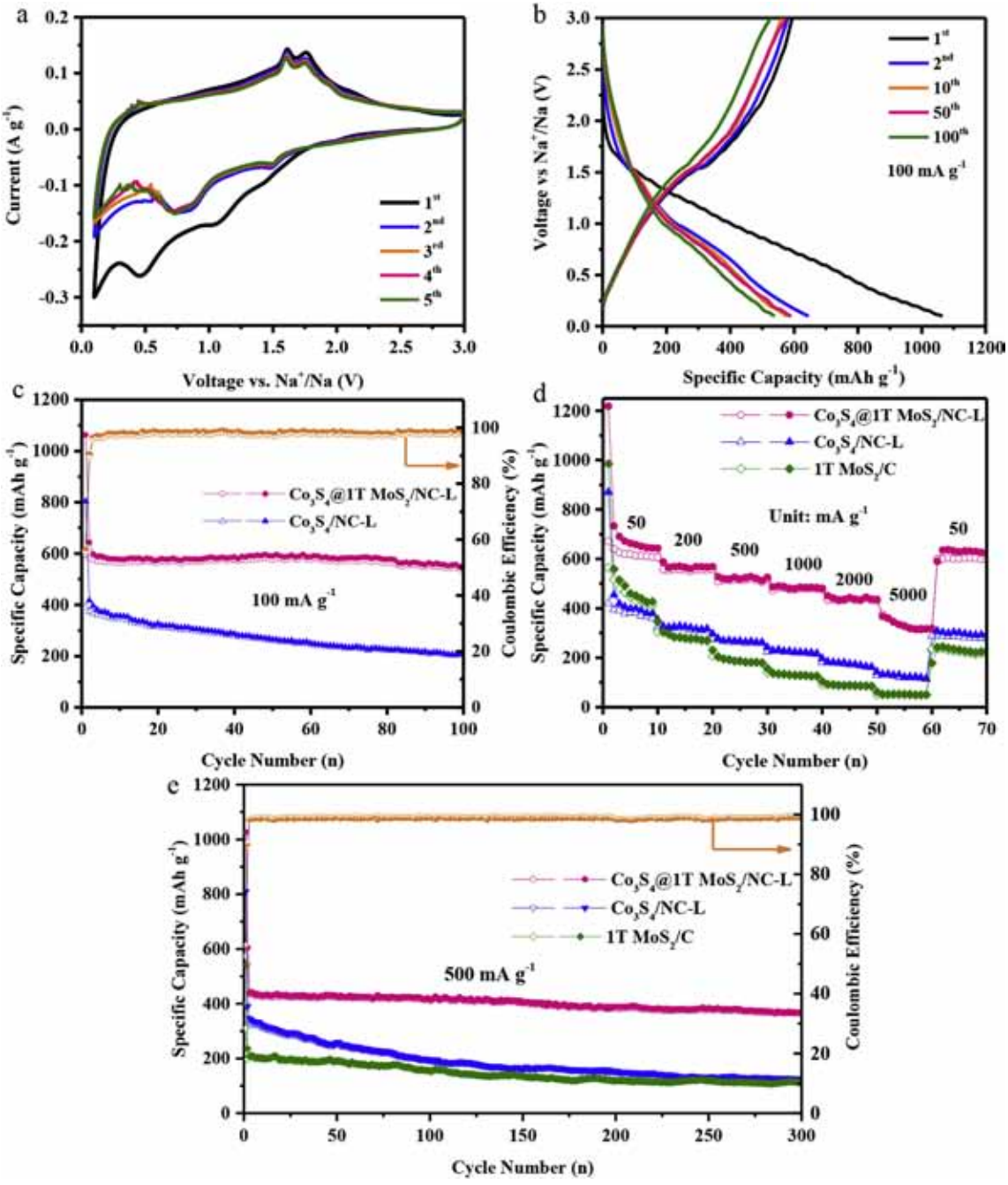

Fig. 4. Electrochemical performances evaluation. a) Representative CV curves for the first five cycles of Co_3S_4@1T MoS_2/NC-L at a scan rate of 0.1 mV s^{-1}. b) GDC profiles of Co_3S_4@1T MoS_2/NC-L at current density of 100 mA g^{-1}. c) Cycling performance of Co_3S_4@1T MoS_2/NC-L and Co_3S_4/NC-L at 100 mA g^{-1}, and the coulombic efficiency (CE) of Co_3S_4@1T MoS_2/NC-L. d) Rate performance of the Co_3S_4@1T MoS_2/NC-L, Co_3S_4/NC-L and 1T MoS_2/C at various current densities. e) Long cycling performance of three samples at 500 mA g^{-1}, and CE of Co_3S_4@1T MoS_2/NC-L.

Co_3S_4/NC-L decreases quickly to 125 mAh g^{-1} and that of MoS_2/C are relatively stable at a low value during 300 cycles. On the one hand, the Co_3S_4@1T MoS_2/NC-L and 1T MoS_2/C show excellent cyclic stability, but the former delivers a specific capacity twice as much as the latter. This is mainly due to the advantages of the hierarchical structure, in which the porous N-doped carbon matrix and expanding 1T MoS_2 layers conduce to ions diffusion and reduction of polarization. Thus, the restricted conversion reaction can produce more reversible capacity. On the other hand, although Co_3S_4@1T MoS_2/NC-L and Co_3S_4/NC-L offer buffering for expansion stress by nitrogen-doped carbon, but their cycling performance is still quite different. This indicates that the volume expansion during sodiation/desodiation process is not the dominating factor for the poor cycling performance. It is deduce that the deep reaction of Co_3S_4 gives rise to severe polysulfide loss, which is responsible for the poor cyclability. In the Co_3S_4@1T MoS_2/NC-L hierarchical nanosheet, the bimetallic sulfides in the N-doped carbon matrix would alternately adsorb the polysulfide and reduce their loss during the conversion reaction into metal and Na_2S.

The Co_3S_4@1T MoS_2/NC-L also exhibits higher specific capacity compared to its single counterpart. Correlatively, the unique hierarchical structure brings out fast reaction kinetics, which could be investigated by CV and EIS measurements. As shown in Fig. 5a, the CV curves of Co_3S_4@1T MoS_2/NC-L at various scan rates range from 0.2 to 2 mV s^{-1} display preserved shape and well-defined peaks. In fact, the

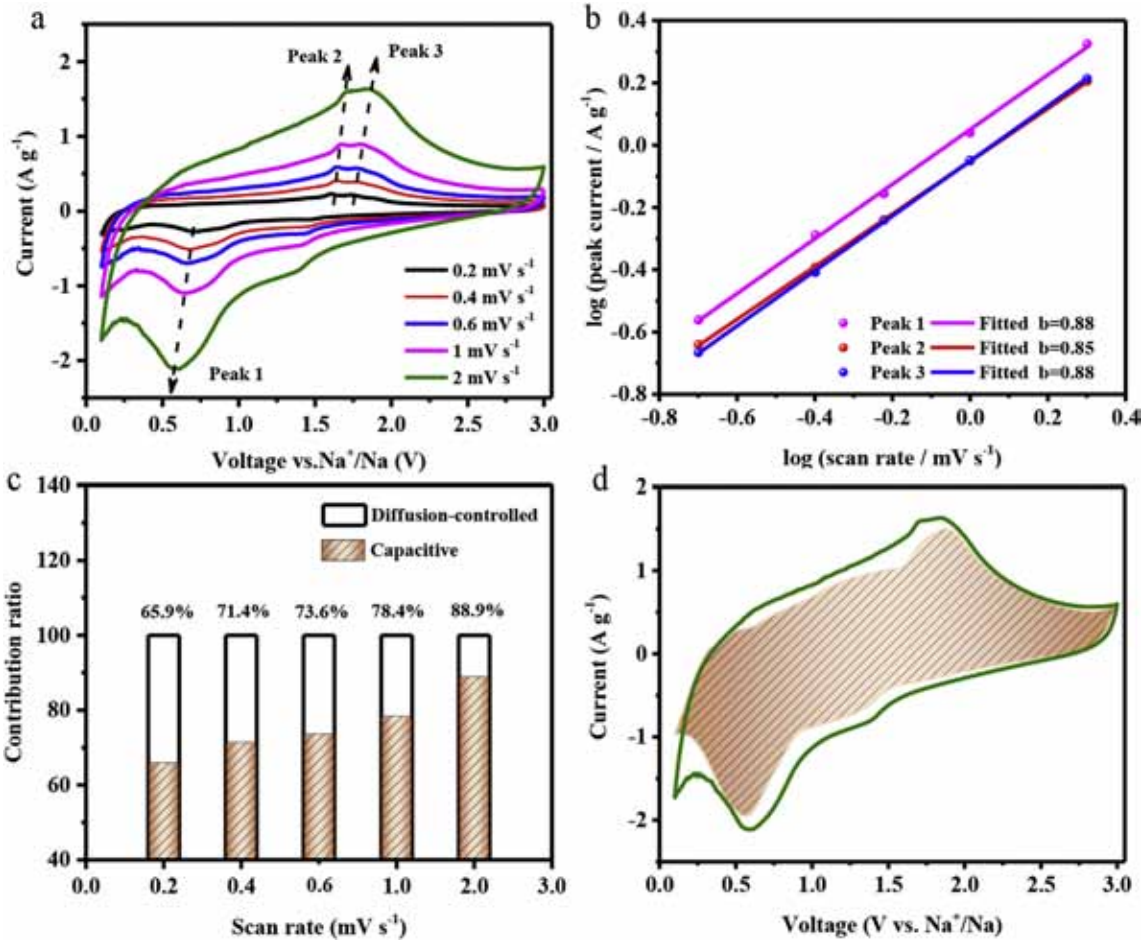

Fig. 5. Electrochemical kinetics investigation of Co_3S_4@1T MoS_2/NC-L electrode. a) CV curves at various scan rates. b) Determination of the b-value according to peak current and scan rate. c) Contribution ratio of the capacitive and diffusion behaviors at various scan rates. d) Separation of the capacitive and diffusion currents in Co_3S_4@1T MoS_2/NC-L at a scan rate of 2 mV s^{-1}.

area of a CV loop indicates joint energy storage from pseudo-capacitive behavior and diffusion-controlled process [16,40]. The corresponding energy storage mechanism can be analyzed by the logarithmic linear relationship of peak current (i) and scan rate (v):

$$\log(i) = \log(a) + b\log(v) \quad (5)$$

Where a, b are the adjustable parameters. The value of b is well-defined: b = 0.5 implies a diffusion-controlled process, and b = 1.0 indicates a pseudo-capacitive behavior [24]. According to **Fig. 5**b, the b values of anodic and cathodic peaks were approached to 1.0, revealing that the pseudo-capacitive behavior dominated the sodium storage process of Co_3S_4@1T MoS_2/NC-L electrode. Specifically, the pseudo-capacitive contribution to sodium storage at different scan rates can be quantitatively evaluated according to the following equation:

$$i(v) = k_1 v + k_2 v^{1/2} \quad (6)$$

where $k_1 \cdot v$ and $k_2 \cdot v^{1/2}$ represent the contributions from pseudo-capacitive behavior and the diffusion-controlled process, respectively [22]. The calculated results are displayed in Fig. 5c. It is obvious that the pseudo-capacitive contribution to sodium storage increases with the scan rate. At a scan rate of 2.0 mV s^{-1} (Fig. 5d), the contribution ratio of pseudo-capacitive behavior is as high as 88.9%. By comparison, the Co_3S_4/NC-L exhibits a weaker pseudo-capacitive behavior, of which contribution ratio is 79.7% at 2.0 mV s^{-1} (Figs. S6a and b). And the 1T MoS_2/C presents a diffusion-controlled electrochemical process due to serious aggregation of nanosheets (Figs. S6c and d). The hierarchical configuration of Co_3S_4@1T MoS_2/NC-L nanosheets offers more active sites for Na^+ adsorption and pseudo-capacitive behavior, thus leading to a high reversible capacity and superior rate performance.

The EIS spectra reveal the redox reaction at the interface and in the electrode, which could be fitted according to an equivalent circuit inset in Fig. 6. The fitting values are given in Table S3. The semicircles in high-medium frequency region are associated with contact resistance (R_f) and charge-transfer resistance (R_{ct}) at the electrode/electrolyte interface, while the slope lines in the low frequency region represent the Warburg impedance (Z_w) related to Na^+ diffusion in electrode [41,42]. The impedance changes of Co_3S_4@1T MoS_2/NC-L for specified cycles were investigated in Fig. 6a. It is found that the resistance (R_f and R_{ct}) decreased at first and then increased with cycling progresses. The reduction of resistance at previous stage is mainly attributed to an activation process of electrode material for sodium storage, while the subsequent increase is caused by the pulverization of electrode and formation of SEI film during the repeated discharge-charge processes. The comparative EIS of three as-prepared electrodes after cycling are also shown in Fig. 6b, where the Co_3S_4@1T MoS_2/NC-L exhibit much smaller resistances (R_f = 40.4Ω and R_{ct} = 148.7Ω) than those of Co_3S_4/NC-L (R_f = 77.8Ω and R_{ct} = 570Ω) and MoS_2/C (R_f = 62.5Ω and R_{ct} = 230.8Ω). The vast active sites from hierarchical configuration and high conductivity of rational N-doped carbon matrix in Co_3S_4@1T MoS_2/NC-L nanosheet are responsible for the reduced resistances. According to the relationship of $Z_w = R + \sigma\omega^{-1/2}$ in low-frequency region, the Warburg factor (σ) can be quantified to demonstrate the ability of Na-ion diffusion in different materials [32,39]. Generally, the smaller σ leads to the faster Na-ion diffusion. In Fig. 6c, the slope (σ) of

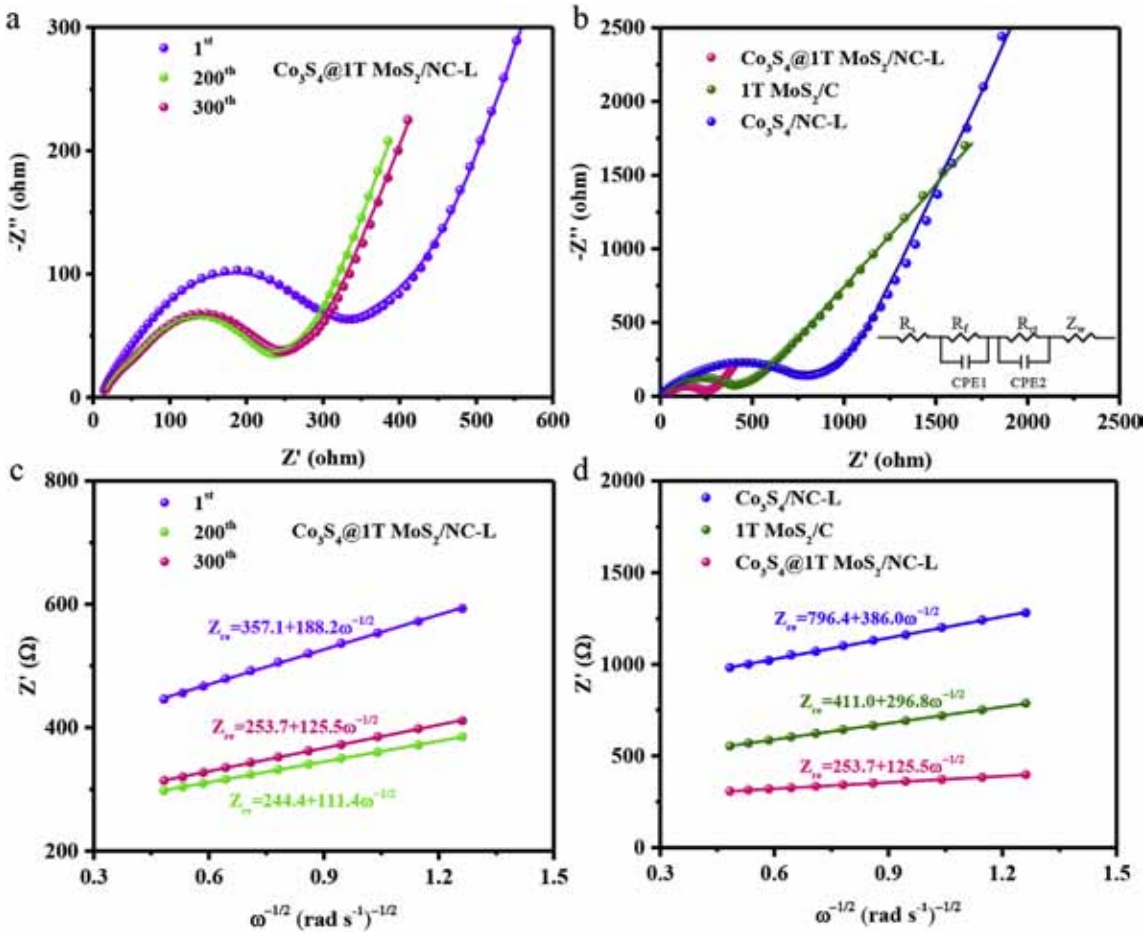

Fig. 6. Electrochemical impedance spectroscopy. a) Nyquist plots of Co_3S_4@1T MoS_2/NC-L for 1st, 200th, 300th cycle. b) Nyquist plots of Co_3S_4@1T MoS_2/NC-L, Co_3S_4/NC-L and 1T MoS_2/C after 300 cycles. c, d) The fitting lines in the low frequency of EIS in a) and b).

Co_3S_4@1T MoS_2/NC-L is smallest among the three as-prepared electrodes, demonstrating the superior Na^+ diffusion in bimetallic sulfide compared to single-phase sulfides. It is obvious that the ability of Na ion transport in Co_3S_4@1T MoS_2/NC-L electrode is slightly changed during cycles (Fig. 6d). Therefore, Co_3S_4@1T MoS_2/NC-L presented enhanced kinetic performance and reversible specific capacity, highlighting the smart integration of bimetallic sulfide into N-doped carbon matrix.

To elucidate the capacity differentiation between bimetallic sulfide and molybdenum sulfide associated with the polarization and kinetics, we studied the Na-ions situations in the MoS_2/Co_3S_4 heterointerface and MoS_2/MoS_2 interlayers by combined DFT and AIMD calculations. The models of 1T MoS_2/Co_3S_4 and 1T MoS_2/MoS_2 bilayers were constructed rationally for DFT calculations, as shown in Fig. 7a and Fig. S7. The model structure is fully optimized before calculating the relevant properties. By comparing the adsorption energies of Na ions in different circumstances, we can obtain the optimal adsorption sites of Na ions in the interface of bilayer. The adsorption energies are evaluated by the following formula:

$$E_{absorb} = E_{bilayer+Na} - E_{bilayer} - E_{Na} \quad (7)$$

Where $E_{bilayer}$ is the energy of the pristine MoS_2/MoS_2 or MoS_2/Co_3S_4 ,$E_{bilayer+Na}$ is the total energy of the Na inserted model, E_{Na} represent the energy of a single Na atom [43]. In Fig. S7, the adsorption energies at different sites of the MoS_2/Co_3S_4 heterointerface present smaller energy barriers than those at MoS_2/MoS_2 interface, indicating the easier migration of sodium ions in the heterointerface. The interaction between the layers and the inserted Na can be reflected by charge density difference. The charge density difference between pristine and Na inserted bilayers can be evaluated by the following formula:

$$\Delta\rho(r) = \rho_{M+Na}(r) - \rho_M(r) - \rho_{Na}(r) \quad (8)$$

$$\Delta\rho(r) = \rho_{M/C+Na}(r) - \rho_{M/C}(r) - \rho_{Na}(r) \quad (9)$$

Whereas $\rho_M(r)$, $\rho_{M/C}$ (r) and $\rho_{Na}(r)$ are the independent electron densities of the pristine MoS_2/MoS_2 , MoS_2/Co_3S_4 and isolated Na, $\rho_{M+Na}(r)$ and $\rho_{M/C+Na}(r)$ are the total charge density of the Na inserted model [35,43]. As presented in Fig. 7b, the red color isosurface represents charge accumulation, while the green isosurface means charge depletion. During the sodiation process, Na atoms first adhere to superficial S atoms and act as a donor of charge transfer for the surrounding S atoms. Obviously, the charge accumulation around S atom in the MoS_2/Co_3S_4 heterointerface is much weaker than that in the MoS_2/MoS_2 interface (Fig. S7c, d). That is to say, the interaction between MoS_2/Co_3S_4 heterointerface and Na atom is weaker, which benefits the free migration of Na atom in the heterointerface [35]. We further investigated the essence of this interaction by electron localization function (ELF). According to Fig. 7c, the ELF value higher than 0.8 could be seen only in the S atom region, while the ELF values around Na atom and other atoms are lower than 0.3. The ELF value distribution pattern demonstrates that Na atom interacts electrostatically with the S atoms on the surface of bilayers and donates the charge to S atoms. Moreover, AIMD simulation was conducted to explore the migration of Na ions between bilayers. The coordinates of Na atoms were extracted at intervals of 50 steps and plotted in the same graph to show the trajectory of Na atoms within 1 ps. From the trajectory, Na atoms show strong mobility at the MoS_2/Co_3S_4

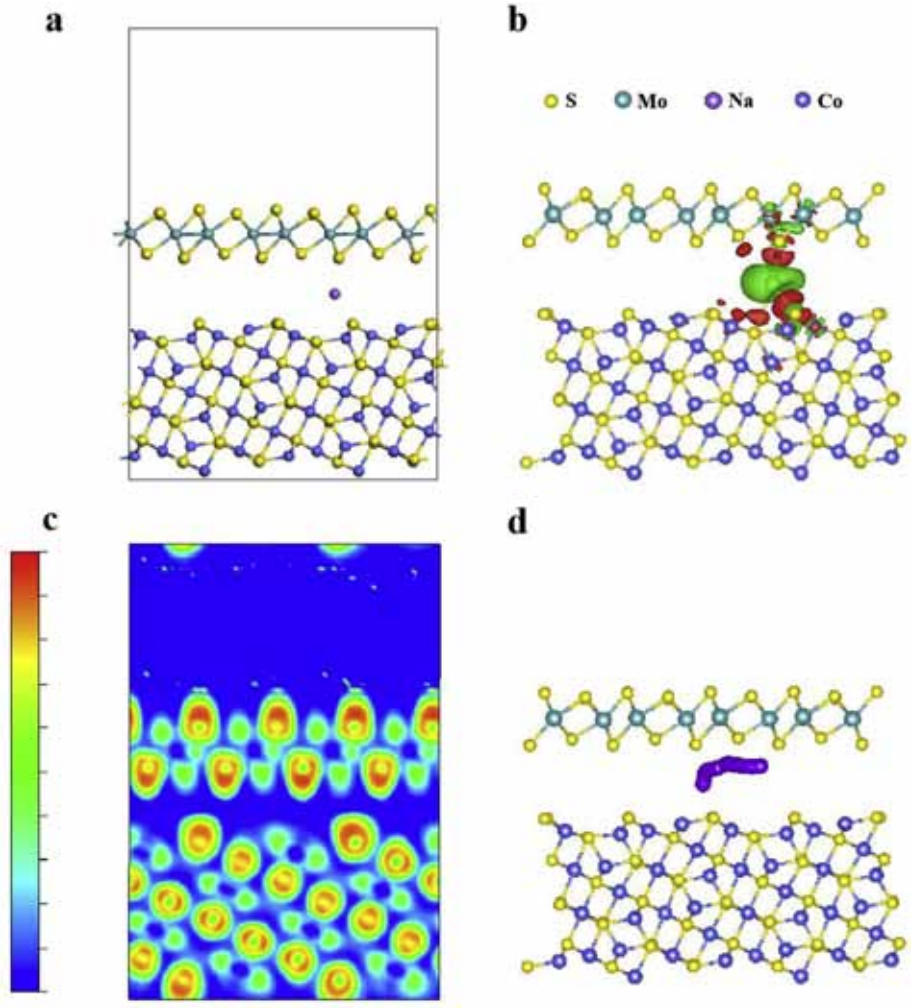

Fig. 7. Density functional theory calculations. a) Optimized structure of the Co_3S_4/MoS_2 heterointerface. b) Charge density difference plot. The green and dark red areas indicate the electron depletion and accumulation. c) ELF plot. The isovalues in ELF plot are 0.5 (outside, green) and 0.55 (inner, red), respectively. d) Na trajectories in Co_3S_4/MoS_2 heterointerface during 10 ps by AIMD simulations at 600 K. Atomic identification: S (yellow), Mo (green), Na (purple), Co (blue). (For interpretation of the references to color in this figure legend, the reader is referred to the Web version of this article.)

heterointerface (Fig. 7d). For the MoS_2/MoS_2 interface, Na atom can only vibrate near the initial site and no obvious ion migration can be observed wherever the initial position of Na atom is (Fig. S7c, d). Therefore, compared with the MoS_2/Co_3S_4 heterointerface, the MoS_2/MoS_2 interface has a more negative effect on the insertion and extraction of Na ions, in accordance with the previous charge difference calculation [35,43]. By comparison, the MoS_2/Co_3S_4 heterointerface presents a mediocre binding to Na atoms and ensures effective charge transfer between them, which makes the bimetallic sulfide system advantageous to sodium storage.

The unique hierarchical architecture and smart integration of bimetallic sulfide into NC matrix are synergistically responsible for the high reversible capacity, superior cyclic stability and excellent rate capability of Co_3S_4@1T MoS_2/NC-L nanosheets. Firstly, the unique hierarchical architecture with nitrogen-doped carbon matrix provides enhanced pseudocapacitance effect and presents small polarization to stimulate the restricted reaction, achieving high capacity. Secondly, the unique hierarchical nanosheets assembled by well-expanding MoS_2 layers and 2D NC matrix promotes the formation of stable SEI layer and high Coulombic efficiency. Thirdly, Thirdly, the restricted conversion reaction leads to partial residual Na_xMoS_2 under the higher cutoff voltage of 0.1 V. Due to the mutual affinity of bimetallic sulfides, the residual Na_xMoS_2 would adsorb the polysulfide and reduce their loss during the conversion reaction of $Na_xCo_3S_4$ and Na_2S/Co. Alternately, the $Na_xCo_3S_4$ formed reversibly in the oxidation process is benefited to stable formation of Na_xMoS_2 and MoS_2. Lastly, the heterogenous interface of bimetallic sulfides provided favorable Na-ion insertion sites and superior ions diffusion kinetics, compared with the single counterpart.

3. Conclusions

In summary, leaf-like hierarchical nanosheets with integration of bimetallic sulfides and N-Doped Carbon (Co_3S_4@1T MoS_2/NC-L) were fabricated by precursor calcination and hydrothermal sulfuration reaction. Co_3S_4/NC-L and 1T MoS_2/C were also prepared under controlled conditions. The compared cycling performance and post-cycled morphology show that some more important factors dominate the capacity decay of metal sulfides except for volume expansion, that is the formation and loss of extensive polysulfide derived from conversion reaction under deep charge/discharge. The higher cutoff voltage (0.1 V vs. 0.01 V) can partly restrict the conversion reaction to Mo/Na_2S, in which the mutual affinity of bimetallic sulfide suppresses the loss of polysulfides, thus improving the cyclic stability of sulfide electrode. Furthermore, electrochemical tests and DFT calculation indicate that Co_3S_4@1T MoS_2/NC-L hierarchical nanosheets present enhanced pseudocapacitance effect and fast Na^+ kinetics. Therefore, the hierarchical nanosheet exhibited high reversible capacity of 595 mAh g^{-1}

at 0.1 A g^{-1} and fine rate capability of 338 mAh g^{-1} at 5 A g^{-1}. Satisfactory charge capacity of 368 mAh g^{-1} was retained at 0.5 A g^{-1} after 300 cycles. This work opens up prospects for the construction of metal sulfides electrodes in electrochemical applications, such as Na/Li ions batteries or electrochemical catalysis.

4. Experimental section

4.1. Material synthesis

Co-ZIF-L precursor was prepared by a facile aqueous reaction of Co $(NO_3)_2{\cdot}6H_2O$ and 2-methylimidazole for 4 h at room temperature, according to the previous report. The violet Co-ZIF-L powder was then calcined at 650 °C for 3 h with a heating rate of 1 °C min^{-1} under N_2 protection to acquire Co/NC-L nanosheets. 0.05 g of as-obtained Co/NC-L nanosheets were dispersed into 30 ml of 0.1 M glucose solution under stirring, then 0.3 g of sodium molybdate ($Na_2MoO_4{\cdot}2H_2O$) and 0.6 g of thiourea were added. The fully mixed solution was transferred into a 50 mL Telfon-lined stainless steel autoclave and kept in an electric oven at 200 °C for 24 h. The Co_3S_4@1T MoS_2/NC-L was collected by centrifugation, washed with water, and dried in a vacuum oven at 60 °C overnight. For comparison, a hydrothermal reaction of Co/NC-L nanosheets and thiourea was conducted to prepare Co_3S_4/NC-L. The 1T MoS_2/C sample was synthesized in the absence of Co/NC-L nanosheets. Other synthesis conditions have remained the same.

4.2. Structure characterization

The morphology of the as-prepared samples was characterized by a scanning electron microscope (Zeiss Sigma 500). FEI Talos 200s microscope equipped with an energy dispersive X-ray detector was used to obtain TEM/HRTEM images, SAED patterns and EDX mappings. XRD patterns were performed on a MiniFlex 600 X-Ray diffractometer with Cu-Ka radiation. ASAP 2460 was used to acquire nitrogen adsorption-desorption isotherms at 77 k. Raman spectra were collected on HORIBA XploRA with a 532 nm laser emitter. An ESCALAB 250Xi X-ray photoelectron spectrometer (ThermoFisher, UK, Al Ka radiation) was employed to characterize the surface chemical state of samples. The Co_3S_4@1T MoS_2/NC-L hierarchical nanosheet was digested into a mixed acid solution and then diluted appropriately to measure the presence of Co, S and Mo elements by inductively coupled plasma mass spectrometry (ICP-MS, Agilent 7800). The molar ratio of Co: S: Mo is about 3.7: 7.0: 1 and the mass ratio of Co_3S_4: MoS_2 is about 2.35: 1.

4.3. Electrochemical measurements

Active materials (Co_3S_4@1T MoS_2/NC-L, Co_3S_4/NC-L, or 1T MoS_2/C), conductive agent (Super-P), and binder (polyimide) were mixed at 7:2:1 and ground in N-methyl-pyrrolidone to form slurry. The working electrodes were prepared by coating the slurry onto a copper foil and dried at 100 °C in vacuum overnight. CR2032-type half cells were assembled by using the working electrodes, Na metal slice as counter electrodes, and fiberglass separators in an Ar-filled glovebox. The electrolyte was 1 M $NaClO_4$ in a mixture of ethylene carbonate/dimethyl carbonate (v/v = 1:1) with 5.0% fluoroethylene carbonate. The electrochemical workstation (PARSTAT™ MC, AMETEK, USA) was used to record cyclic voltammetry (CV) profiles and electrochemical impedance spectra (EIS) ranging from 100 kHz to 0.1 Hz. Galvanostatic charge-discharge measurements with voltage window of 0.1-3.0 V were conducted on a multichannel battery tester (Land CT 2001A). The working electrode has a diameter of 12 mm and the mass loading of active material is 0.8-1.0 mg cm^{-2}.

4.4. Computational methods

The role of bimetallic sulfides (1T MoS_2/Co_3S_4) heterointerface on Na ion storage was studied by density functional theory (DFT) calculations. For comparison, the models of 1T MoS_2/MoS_2 interface were also been established. All the DFT calculations were performed under the general gradient approximation (GGA) using the Perdew-Burke-Ernzerhof (PBE) as function implemented in the Vienna ab initio simulation package (VASP) [44–46]. Since the total number of atoms in heterointerface models reaches 446, 1 × 1 × 1 K-point mesh was selected in the DFT calculation. And the K-point mesh for 1T MoS_2/MoS_2 interface model was 5 × 5 × 1 [47]. After rigorous testing, the cutoff energy was set to 500 eV, atomic coordinates and lattice sizes were fully optimized until 0.01 eV/Å in force and 10^{-5} eV per atom in energy. The van der Waals correction was implemented in the D3 scheme [43]. In addition, AIMD simulation were carried out to study the diffusion kinetics of Na ions in the interfaces with a total simulation time of 1ps. A timestep of 1 fs was chosen and the simulation temperature was set to 400 K using a Nose thermostat.

Acknowledgement

This work is supported by National Natural Science Foundation of China (Grant No. 51702272); Natural Science Foundation project of Fujian Province, China (No. 2018J01519); The Talents Introduction Program of Xiamen University of Technology, China (E2016144). This work is supported partially by Natural Science Foundation of Beijing Municipality (L172036), Joint Funds of the Equipment Pre-Research and Ministry of Education; China (6141A020225), Par-Eu Scholars Program, China, Science and Technology Beijing 100 Leading Talent Training Project, China; Beijing Municipal Science and Technology Project, China (Z161100002616039); The Fundamental Research Funds for the Central Universities,China (2016JQ01, 2017ZZD02); The NCEPU “Double First-Class" Graduate Talent Cultivation Program, China.

Appendix A. Supplementary data

Supplementary data to this article can be found online at https://doi.org/10.1016/j.nanoen.2019.05.040.

References

[1] P.K. Nayak, L. Yang, W. Brehm, P. Adelhelm, Angew. Chem. Int. Ed. 57 (2018) 102–120.
[2] V. Palomares, P. Serras, I. Villaluenga, K.B. Hueso, J. Carretero-González, T. Rojo, Energy Environ. Sci. 5 (2012) 5884–5901.
[3] S.Y. Hong, Y. Kim, Y. Park, A. Choi, N.-S. Choi, K.T. Lee, Energy Environ. Sci. 6 (2013) 2067–2081.
[4] B. Jache, P. Adelhelm, Angew. Chem. 126 (2014) 10333–10337.
[5] M. Shirpour, J. Cabana, M. Doeff, Energy Environ. Sci. 6 (2013) 2538–2547.
[6] M. Shirpour, J. Cabana, M. Doeff, Chem. Mater. 26 (2014) 2502–2512.
[7] C. Zhao, C. Yu, M. Zhang, H. Huang, S. Li, X. Han, Z. Liu, J. Yang, W. Xiao, J. Liang, X. Sun, J. Qiu, Adv. Energy Mater. 7 (2017) 1602880.
[8] Y. Liu, Z. Cheng, H. Sun, H. Arandiyan, J. Li, M. Ahmad, J. Power Sources 273 (2015) 878–884.
[9] Y. Xiao, S.H. Lee, Y.-K. Sun, Adv. Energy Mater. 7 (2017) 1601329.
[10] W. Sun, X. Rui, D. Zhang, Y. Jiang, Z. Sun, H. Liu, S. Dou, J. Power Sources 309 (2016) 135–140.
[11] R. Tian, Y. Zhou, H. Duan, Y. Guo, H. Li, K. Chen, D. Xue, H. Liu, ACS Appl. Energy Mater. 1 (2018) 402–410.
[12] J. Lu, G. Xia, S. Gong, C. Wang, P. Jiang, Z. Lin, D. Wang, Y. Yang, Q. Chen, J. Mater. Chem. 6 (2018) 12613–12622.
[13] M. Acerce, D. Voiry, M. Chhowalla, Nat. Nanotechnol. 10 (2015) 313.
[14] R. Kappera, D. Voiry, S.E. Yalcin, B. Branch, G. Gupta, A.D. Mohite, M. Chhowalla, Nat. Mater. 13 (2014) 1128.
[15] Z. Lei, J. Zhan, L. Tang, Y. Zhang, Y. Wang, Adv. Energy Mater. 8 (2018) 1703482.
[16] C. Zhao, C. Yu, B. Qiu, S. Zhou, M. Zhang, H. Huang, B. Wang, J. Zhao, X. Sun, J. Qiu, Adv. Mater. 30 (2018) 1702486.
[17] X. Li, W. Li, M. Li, P. Cui, D. Chen, T. Gengenbach, L. Chu, H. Liu, G. Song, J. Mater. Chem. 3 (2015) 2762–2769.
[18] X. Xu, R. Zhao, W. Ai, B. Chen, H. Du, L. Wu, H. Zhang, W. Huang, T. Yu, Adv. Mater. 30 (2018) 1800658.
[19] G. Wang, J. Zhang, S. Yang, F. Wang, X. Zhuang, K. Müllen, X. Feng, Adv. Energy Mater. 8 (2018) 1702254.
[20] X. Hu, Y. Li, G. Zeng, J. Jia, H. Zhan, Z. Wen, ACS Nano 12 (2018) 1592–1602.

[21] Y. Cai, H. Yang, J. Zhou, Z. Luo, G. Fang, S. Liu, A. Pan, S. Liang, Chem. Eng. J. 327 (2017) 522–529.
[22] G. Fang, Z. Wu, J. Zhou, C. Zhu, X. Cao, T. Lin, Y. Chen, C. Wang, A. Pan, S. Liang, Adv. Energy Mater. 8 (2018) 1703155.
[23] R. Chen, J. Yao, Q. Gu, S. Smeets, C. Baerlocher, H. Gu, D. Zhu, W. Morris, O.M. Yaghi, H. Wang, Chem. Commun. 49 (2013) 9500–9502.
[24] X. Li, W. Zhang, Y. Feng, W. Li, P. Peng, J. Yao, M. Li, C. Jiang, Electrochim. Acta 294 (2019) 173–182.
[25] M. Wu, J. Zhan, K. Wu, Z. Li, L. Wang, B. Geng, L. Wang, D. Pan, J. Mater. Chem. 5 (2017) 14061–14069.
[26] Q. Liu, X. Li, Q. He, A. Khalil, D. Liu, T. Xiang, X. Wu, L. Song, Small 11 (2015) 5556–5564.
[27] X. Li, G. Wu, X. Liu, W. Li, M. Li, Nano Energy 31 (2017) 1–8.
[28] L. Chu, M. Li, X. Li, Y. Wang, Z. Wan, S. Dou, D. Song, Y. Li, B. Jiang, RSC Adv. 5 (2015) 49765–49770.
[29] X. Fan, P. Xu, D. Zhou, Y. Sun, Y.C. Li, M.A.T. Nguyen, M. Terrones, T.E. Mallouk, Nano Lett. 15 (2015) 5956–5960.
[30] Y. Liu, C. Xiao, M. Lyu, Y. Lin, W. Cai, P. Huang, W. Tong, Y. Zou, Y. Xie, Angew. Chem. 127 (2015) 11383–11387.
[31] J. Yang, K. Wang, J. Zhu, C. Zhang, T. Liu, ACS Appl. Mater. Interfaces 8 (2016) 31702–31708.
[32] P. Ge, H. Hou, X. Cao, S. Li, G. Zhao, T. Guo, C. Wang, X. Ji, Adv. Sci. 5 (2018) 1800080.
[33] P. Ge, H. Hou, S. Li, L. Huang, X. Ji, ACS Appl. Mater. Interfaces 10 (2018) 14716–14726.
[34] H. Li, X. Qian, C. Xu, S. Huang, C. Zhu, X. Jiang, L. Shao, L. Hou, ACS Appl. Mater. Interfaces 9 (2017) 28394–28405.
[35] X. Lei, K. Yu, R. Qi, Z. Zhu, Chem. Eng. J. 347 (2018) 607–617.
[36] P. Cheng, K. Sun, Y.H. Hu, Nano Lett. 16 (2016) 572–576.
[37] H. Huang, Y. Cui, Q. Li, C. Dun, W. Zhou, W. Huang, L. Chen, C.A. Hewitt, D.L. Carroll, Nano Energy 26 (2016) 172–179.
[38] M. Acerce, D. Voiry, M. Chhowalla, Nat. Nanotechnol. 10 (2015) 313–318.
[39] Y. Wang, W. Kang, D. Cao, M. Zhang, Z. Kang, Z. Xiao, R. Wang, D. Sun, J. Mater. Chem. 6 (2018) 4776–4782.
[40] P. Ge, C. Zhang, H. Hou, B. Wu, L. Zhou, S. Li, T. Wu, J. Hu, L. Mai, X. Ji, Nano Energy 48 (2018) 617–629.
[41] X. Li, Y. Feng, M. Li, W. Li, H. Wei, D. Song, Adv. Funct. Mater. 25 (2015) 6858–6866.
[42] X. Li, G. Wu, J. Chen, M. Li, W. Li, T. Wang, B. Jiang, Y. He, L. Mai, Appl. Surf. Sci. 392 (2017) 297–304.
[43] J. Wu, Z. Lu, K. Li, J. Cui, S. Yao, M. Ihsan-ul Haq, B. Li, Q.-H. Yang, F. Kang, F. Ciucci, J.-K. Kim, J. Mater. Chem. 6 (2018) 5668–5677.
[44] P.E. Blöchl, Phys. Rev. B 50 (1994) 17953–17979.
[45] G. Kresse, J. Furthmüller, Phys. Rev. B 54 (1996) 11169–11186.
[46] G. Kresse, D. Joubert, Phys. Rev. B 59 (1999) 1758–1775.
[47] S. Grimme, J. Comput. Chem. 27 (2006) 1787–1799.